



Fractal dimension of cathode spots in a high-current vacuum arc thruster

Etienne Michaux*, Alfio E. Vinci, Stéphane Mazouffre

CNRS, Institut de Combustion, Aérothermique, Réactivité et Environnement (ICARE), 1C avenue de la recherche scientifique, Orléans, 45071, France

ARTICLE INFO

Keywords:

Vacuum arc thruster
Fractals
Metallic materials
High current
Pulsed discharge
Electric propulsion for spacecraft

ABSTRACT

The fractal dimension of cathode spots occurring in the discharge of a high-current vacuum arc thruster (VAT) are determined according to the Minkowski–Bouligand method. Photographs taken during operation of a 30 W VAT allowed observation of spots distribution over the surface depending on the cathode material. A machine learning model as well as a heuristic analysis permit to outline that work function, cohesive energy and ionization energy of the cathode material are the main driver in the magnitude of fractal dimension and total surface area covered by the spots.

1. Introduction

The formation of ramified patterns has been observed for a long time in the case of electrical breakdowns at atmospheric pressure [1]. Similar patterns have also been seen on traces left by a vacuum arc on a stainless steel plate [2]. However, the mechanism at the origin of these patterns is very different. Concerning atmospheric pressure electrical breakdowns, these patterns are the pathways of charge-flow in the propagation medium of the arc. This is well exemplified by the phenomenon of lightning during a storm. When it comes to vacuum arcs though, those patterns are seen on the cathode surface and are formed through the ignition and extinction of plasma emission sites. These sites, named cathode spots, are distributed on the cathode surface in accordance with random walk patterns [3,4] leading to the formation of tree-like structures. These structures can be described as objects with non-integer dimension, namely fractals.

Although the fractal nature of cathode spots has already been the subject of several studies [2,4–6], most experimental arrangements involved low-current long duration vacuum arcs. Consequently little is known today on the fractal nature of high-current vacuum arcs. Recent application of vacuum arcs in spacecraft propulsion tends to maximize the current while reducing the discharge duration [7,8]. By doing so, the thruster maximizes the instantaneous thrust while avoiding thermal issues at the electrodes. These systems, called Vacuum Arc Thrusters (VAT), rely on a vacuum arc between two electrodes. The cathode material is ionized, accelerated and ejected at velocities up to 50 km s^{-1} [9], leading to thrust generation in the opposite direction. This technology presents inherent advantages regarding miniaturization, simplicity and reliability through the use of a solid metal propellant. However, at this stage, the formation of the arc, its dynamics and the subsequent plasma acceleration mechanism remain

poorly understood. Probing in depth the physics of VATs and gathering data is therefore needed to propose more efficient solutions with longer lifetime able to meet the requirements of a wide range of space missions.

Arcs and cathode spots certainly play a major role in thrust and specific impulse generation by VATs. In the present study we determine the fractal dimension of the cathode spot structures for different cathode materials of a low-power high-current VAT. Calculations are performed using the Minkowski–Bouligand method. The approach relies on photographs taken during operation of the VAT, the characteristics of the latter being given in [Experimental arrangement](#) section, along with a description of the setup. The way the photographs are processed and how the fractal dimension is retrieved are detailed in [Method and results](#) section. The fractal dimension of the cathode spot structures is then studied by investigating the influence of the material physical properties using statistical and machine learning approaches in [Influence of material properties](#) section. Eventually, [section 6](#) outlines the conclusions.

2. Experimental arrangement

2.1. The PJP thruster

The VAT under study is the Plasma Jet Pack (PJP) developed by the COMAT French company. This 30 W-class VAT generates a high current vacuum arc through the cyclic discharge of a capacitor bank. The cathode to anode voltage is continuously set to 250 V. A triggering system applies a few kV pulse on the cathode surface lasting a few hundreds of ns. This pulse allows ignition of the plasma

* Corresponding author.

E-mail address: etienne.michaux@cnrs-orleans.fr (E. Michaux).

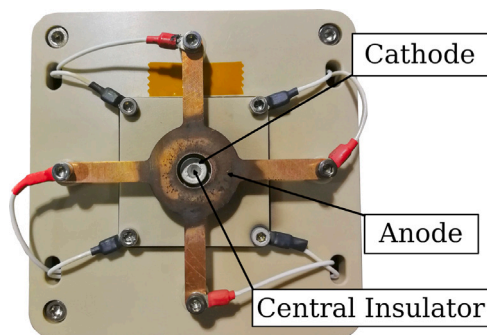


Fig. 1. Plasma Jet Pack thruster: front view.

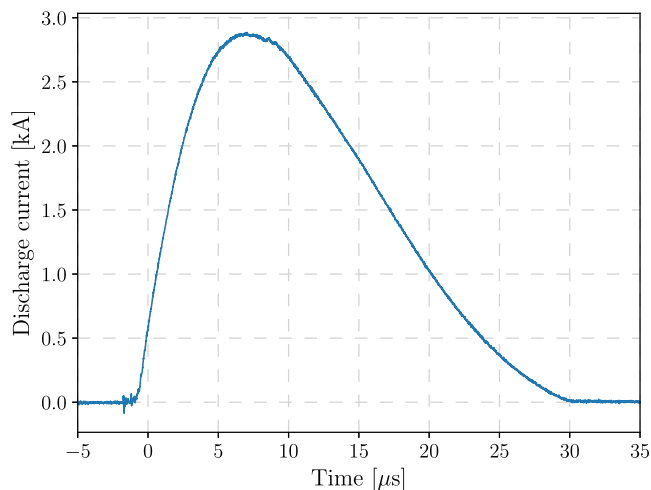


Fig. 2. Typical PJP discharge current waveform during one pulse (Ti).

through an explosive process occurring on a surface region named cathode spot [10]. The high voltage applied during the trigger phase initiates a breakdown by field emission [11] that is followed by a spark and then an arc. During VAT operation, a thin metallic layer deposits on the central insulator that separates the triggering system and the cathode. Ignition of the discharge is then easier as the breakdown occurs through the conductive layer. Note that when the deposited layer is thick it becomes more difficult to vaporize and the thruster no longer operates properly [12]. After the trigger is switched-off, the arc is forced to propagate to the anode through the existing metal vapor. This second arc discharge allows roughly 3 to 4 kA to flow between the two electrodes with the present configuration. The discharge current waveform obtained with a titanium cathode is exemplified in Fig. 2. Overall, the energy released over 25 μs into one single PJP discharge reaches a few J. Measurements presented in this contribution have been performed with a copper anode and various cathode materials, namely simple metals such as titanium, aluminum, iron and copper, as well as metallic alloys like brass (63% Cu–37% Zn) and nichrome (80% Ni–20% Cr). All cathodes were new before photographs were taken.

Fig. 1 shows the front view of a laboratory version of the PJP. The 4-legs electrode is the annular copper anode. The cathode corresponds to the gray center-mounted hollow cylinder. The latter is screwed onto a copper plate directly wired to the capacitor bank. The gap in the axial direction between the cathode and the anode is approximately 1 cm. The trigger electrode is a tiny metal tip placed exactly on the thruster axis and separated from the cathode with the central insulator. The PJP target performance and characteristics are given in Table 1 for the inclined reader.

Table 1

PJP thruster target performance and characteristics.		
Power	0–30	W
Thrust to power	10	$\mu\text{N W}^{-1}$
Average thrust at 30 W	300	μN
Specific impulse	2500	s
Total impulse	400	N s
Overall mass	1	kg
Overall volume	1	U

2.2. Experimental arrangement

Experiments have been performed in the EPIC-2 vacuum chamber of the laboratory. This chamber is a stainless steel cylinder 54 cm in radius and 104 cm in length, for an approximate capacity of 240 l. Two 2200 l s^{-1} (N_2) magnetically levitated STP-iS2207 turbomolecular pumps from Edwards are placed on top of the chamber. Those pumps, evacuated through a $110 \text{ m}^3 \text{ h}^{-1}$ dry primary pump (Edwards GV110), permit to keep a background pressure of 10^{-6} mbar during thruster operation. The pressure is monitored with a Pfeiffer PBR260 Pirani/Bayard-Alpert pressure gauge.

EPIC-2 is also equipped with several electrical feedthroughs, for both in-situ diagnostics and thruster power supply. Those feedthroughs are mostly composed of BNC or SubD connectors. Two Kodial (Borosilicate 7056) glass windows allow visual inspection of the thruster.

The experimental setup is depicted in Fig. 3. In EPIC-2, the PJP is placed on a horizontal plate screwed on a rail. This mounting allows adjustment of the distance to the front window, depending on the experiment to be performed. In this case the distance is set to have the cathode surface filling the whole camera field of view. In doing so, the accuracy of the Minkowski–Bouligand algorithm is increased, see Section 3.2. Moreover one gets a complete view of all the cathode spots that can appear during a discharge. As the cathode surface is small, the PJP has been placed as closed as possible to the window. The distance was then fixed to 30 cm for this experimental campaign.

The camera was a Nikon D40 with a 6 Mpx CMOS sensor, which has been equipped with a Sigma 180 mm F2.8 macro lens. In order to increase the magnification ratio, a Kenko TELEPLUS MC7 AF 2x lens as well as two extension tubes have been added as shown in Fig. 3. The exposure time has been set to 1 s so that all the light emitted during the discharge is received by the sensor. In this way, one can extract the properties of all the cathode spot traces over the entire surface during a PJP pulse. As spots emit a large amount of light, the camera ISO has been set to the lowest option available, i.e. 200, thus limiting the sensor light sensitivity. To achieve an appropriate exposure, a neutral density filter with an attenuation factor of 10 has been mounted ahead of the lenses, as illustrated in Fig. 3. In order to avoid variations in the camera alignment while manually operating the shutter, the sensor has been triggered by means of an infrared remote control synchronized with the PJP duty cycle. The same setup and procedure apply for all cathode materials. After changing of the cathode, the thruster and the optical system were realigned to warranty sharp high-resolution images.

In total, 410 photographs have been used in this work. For each cathode material, the dataset includes about 50 pictures, a large enough number to ensure correct outcomes of a statistical analysis.

3. Fractal dimension

3.1. Image preprocessing

Fig. 4 shows a photograph of PJP discharge triggered with a titanium cathode along with physical boundaries of both the cathode and the anode. The dendritic nature of the plasma emission sites and the arc overall shape are obvious by the naked eye in Fig. 4. The luminous light blue structures extend from the inner edge of the cathode to the

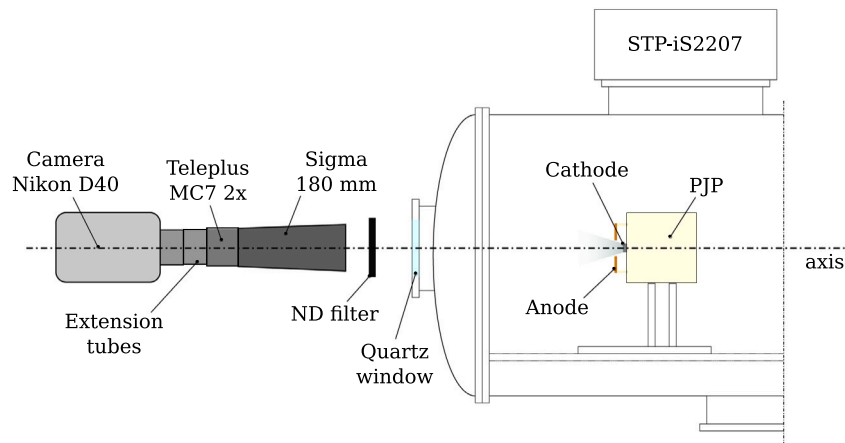


Fig. 3. Schematic of the experimental setup.

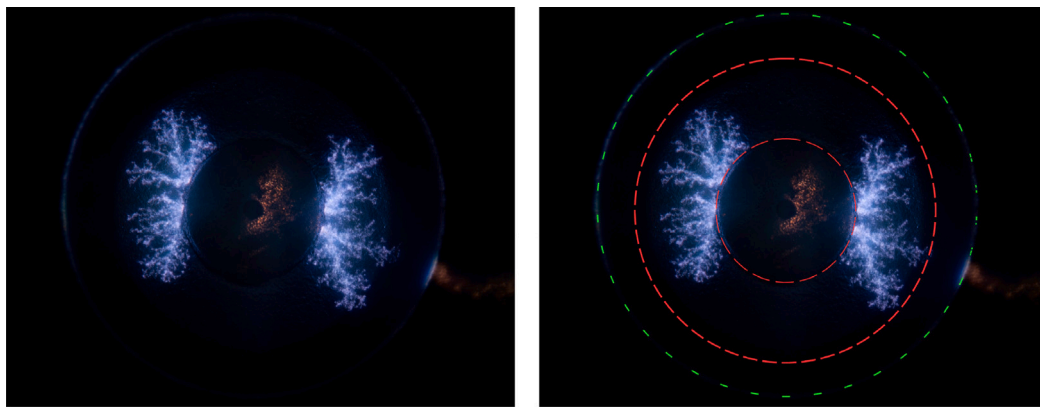


Fig. 4. Raw photograph of a vacuum arc on a titanium cathode (left). Red densely-dashed and green loosely-dashed lines indicate cathode and anode boundaries respectively (right).

outer edge. One can note dendrites are more sparse and less luminous near the outer edge of the cathode. The cathode resembles a hollow disk when seen from the front. The center of this disk corresponds to the insulator, where a reddish glow is observed as can be seen in the image of Fig. 4. In this photograph, parts of the internal edge of the anode are illuminated. A large bright circle can be seen in Fig. 4. Since these regions are facing the cathode arcs, light may originate from reflection. It is for instance the case for the left region. The reddish glow at the bottom right part certainly corresponds to a so-called anode mode [13].

An image processing algorithm must be able to identify the structure of interest prior to analysis. Here, the structure is the cathode spot traces, i.e. points with high light intensity. However, other bright zones appear in the pictures as previously discussed. It is then crucial to remove those parasitic elements before image analysis as they can perturb data treatment and lead to erroneous results and conclusions. This situation is exemplified in Fig. 5. First, for most VAT discharges anode modes are observed [13]. In short, this leads to a glow in the anode region. The anodic arc area is circled in yellow in Fig. 5. Second, a glow is visible on the center-mounted insulator due to a plasma discharge on its surface. The metal deposition that accumulates on the insulator during PJP operation is ionized at the early stage of the discharge when the high voltage is applied. This area, which is circled in red in Fig. 5, is not considered as part of the arc discharge as ionized particles do not originate from the cathode material in that case [14]. Last, the cathode spots illuminate the outer edge of the insulator, green rectangle and enlarged image in Fig. 5. This zone could be mistaken with the cathode spots by the algorithm and must be removed. The three described areas have been manually covered with black pixels by

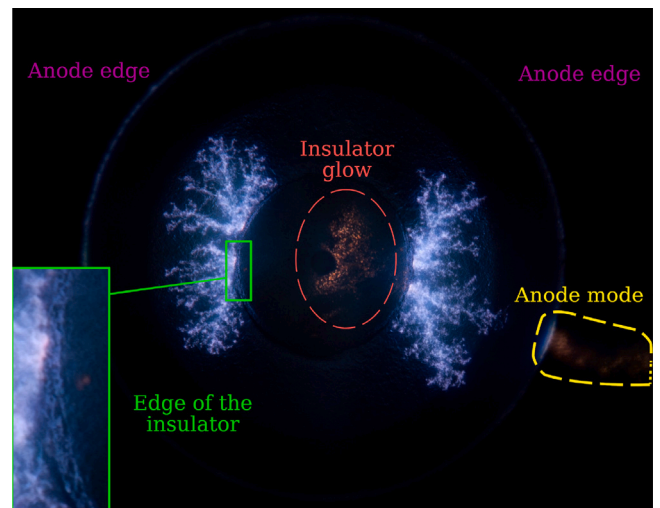


Fig. 5. Unwanted zones in a photograph of a vacuum arc. Image in Fig. 4 is used as a reference.

means of an image manipulation program in this work. Note the inner edge of the anode, see Fig. 5, is also removed.

The light halo generated by the arc, see Fig. 5, must also be treated before image processing. This halo is the diffuse light seen around the cathode spots. It results from the intense light emission of the arc.

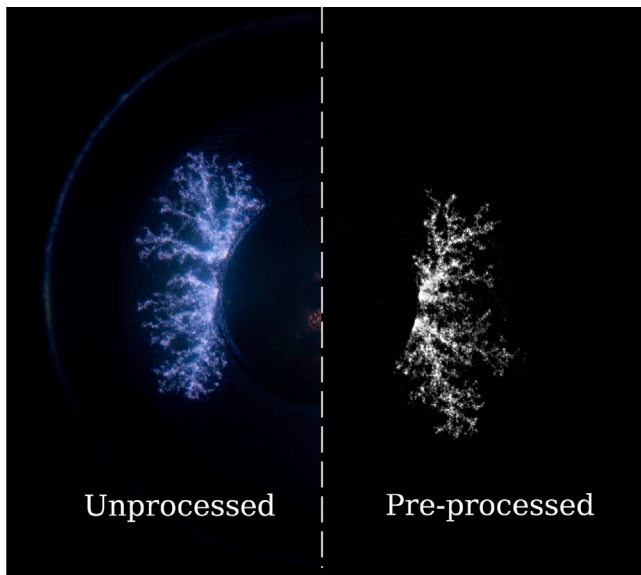


Fig. 6. Vacuum arc image before (left) and after (right) preprocessing.

Misalignment of the camera and optics also favors its appearance. During image processing the picture is transformed into a binary matrix, indicating whether the pixel belongs to the set of cathode spots or not. This halo being especially intense in the space between the branches of the structure, the fractal nature of the arcs is lost if the halo is kept. In other words, keeping the halo would distort the calculation of the fractal dimension.

To decrease the impact of the luminous halo and extract the cathode spot traces, the solution is to fine tune white balance and tonal curves of each photograph. This operation permits to sharpen the color difference between the trace and the halo. The color components of the halo are strongly desaturated with regard to the ones of the spots, reducing its brightness. Afterward conversion to gray scale is performed. It results in a gray-scale picture of the arc discharge in which the spot traces are sharper than in the original picture, without any additional numerical filter. Outcome of preprocessing is illustrated in Fig. 6 for the vacuum arc image presented in Fig. 4.

3.2. Minkowski–Bouligand method

Before determining the fractal dimension, the image must be turned into a binary matrix. In our study each pixel of a preprocessed image is associated with a value that varies between 0 and 1 according to a 8-bit gray scale. This numerical value is given by the normalized brightness of the pixel. A brightness threshold is then defined for each material. Above the threshold, the pixel is considered as part of the spot pattern and the value of 1 is assigned to the pixel. Below the threshold the value 0 is assigned to the pixel as it does not belong to the pattern. The result is a binary matrix that is used for the calculation of the fractal dimension D of the spot structure. Threshold is given in Table 2 for the different cathode materials. In order to assess the threshold, preprocessed images in gray scale are compared with binary images. The threshold is defined as the value that gives a binary image representative of the real image. When the threshold is low, the overall aspect of the image is changed. When it is high the image is smoother and the dendritic geometry tends to vanish. A precise value is hard to define for the threshold, fortunately it has a moderate impact on the fractal dimension. In the case of Ti for instance, the change in D is only 0.02 when considering the lowest and the highest value of the threshold, which is below the standard deviation for D , see Section 3.3.

To recover the fractal dimension of the cathode spot luminous traces, the Minkowski–Bouligand method, also known as box counting

Table 2
Threshold for different cathode materials.

Material	Threshold
Ti	0.30
Al	0.25
Ni-Cr	0.40
Fe	0.35
Brass	0.48
Cu	0.40

Table 3
Mean fractal dimension and standard deviation for different cathode materials.

Material	D	σ_D
Ti	1.450	0.028
Al	1.329	0.038
Ni-Cr	1.326	0.034
Fe	1.288	0.019
Brass	1.198	0.032
Cu	1.145	0.021

method, has been used. According to this method a fractal S is covered with an evenly spaced grid and the number of squares required to cover S is counted. The dimension is calculated by evaluating how this number changes as the grid is made finer. The Minkowski–Bouligand dimension, or box-counting dimension, is defined as:

$$\dim_{\text{box}}(S) = \lim_{\epsilon \rightarrow 0} \frac{\log N(\epsilon)}{-\log \epsilon} \quad (1)$$

where $N(\epsilon)$ is the number of squares of side length ϵ required to cover the structure [15,16]. The box counting process is interrupted when ϵ equals the size of the camera pixel. However, as the camera sensor contains 6×10^6 pixels, multiple iterations can still be made before reaching this limit. As the mesh is refined, N is calculated for each step. Eventually the $\log(N)$ versus $-\log(\epsilon)$ curve is plotted and a line is fitted to the dataset. The slope of the linear fit gives the fractal dimension. Details about the computation methodology can be found in Ref. [17] for the inclined reader. Fig. 7 shows the curve obtained for the image in Fig. 4 along with the associated linear fit. As can be seen points are well aligned. The R^2 value is 0.996. On this example the fractal dimension is $D = 1.448$, a value close to the dimension of the Viscek snowflake and the quadratic Von Koch curve type 1.

3.3. Fractal dimension

The mean fractal dimension determined with the box-counting algorithm for each VAT cathode material along with the associated standard deviation are presented in Table 3, sorted in ascending order. As can be seen, the standard deviation remains low for all materials with a relatively constant magnitude. Moreover, except for Al and NiCr datasets, each element has a D value outside the $D \pm \sigma_D$ interval of the other elements. It means that there is a significant difference between the fractal structures of all studied materials. Titanium has the highest D whereas copper exhibits the lowest.

It is known, referenced and usually admitted that the cathode spot patterns depends on the surface condition, i.e. the degree of contamination by oxides [18–20] and the roughness [2,4,5]. In order to verify if the fractal dimension is impacted by the cathode surface properties under our arc condition, experiments have been performed with a brand new Ti cathode and a worn-out cathode exposed to more than 10^4 discharges. A set of 100 photographs has been collected and analyzed for the two cathodes. The fractal dimension is given in Table 4. It results that there is no significant differences between the two values as they overlap when accounting for the standard deviation. Two explanations can be proposed then. Either the surface roughness and state of the two cathodes are comparable in spite of a very different

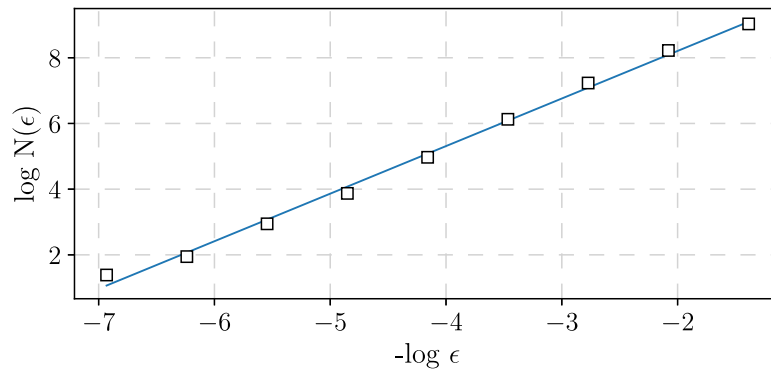


Fig. 7. Plot for fractal dimension of vacuum arc image shown in Fig. 4 obtained with the box-counting method: $D = 1.448$.

Table 4
Fractal dimension and covered area for a fresh and a worn titanium cathode.

Cathode	D	σ_D	S [mm ²]	σ_S
Ti new	1.45	0.03	4.2	0.4
Ti old	1.42	0.03	4.6	0.5

exposure to the high current plasma discharge, or there is indeed no influence of the surface roughness on D . The second explanation is more likely as the erosion of the “old” cathode was clearly noticeable with a change in the geometry. The fractal dimension of the vacuum arc cathode spots pattern would therefore mostly depends on the material properties and contamination by oxides. There is unfortunately no way to quantify the degree of contamination by oxygen with the present experimental setup. We ensured that the operating frequency and the background pressure were the same for all cathodes, respectively 1 Hz and 10^{-6} mbar. Moreover, the thruster is fired during about 2 min (~100 pulses) after installation in the vacuum chamber to clean the cathode and anode surface.

3.4. Covered surface area

The cathode material has a strong impact on D as previously demonstrated. It is also obvious from the pictures that the area covered by the spots depends upon the material. Fig. 8 shows photographs of the vacuum arc cathode spots for the six different cathode materials. While for titanium the spots show large branches that separate into small dendrites, for copper and brass the sub-structures are much less developed and they form small and compact islands, especially for copper. A common point between all images is that the spots seem to develop and propagate mainly in the radial direction with the external edge of the central insulator as origin. It should be noted that when more than one spot is active, which is the case here, the direction of new ignitions is influenced by the magnetic field of the current paths (active spots) [21,22].

From the binary matrix of an arc, one can easily determine the surface area covered by the spots. Scaling the picture allows to determine the exact size of one pixel. Then, the total area of cathode spots is given by the number of pixels associated with value 1 in the binary matrix times the area that corresponds to one single pixel. Results are presented in Table 5, with area sorted in descending order.

The largest spot area is obtained with Ti whereas the smallest area is obtained with Cu. In fact the fractal dimension D and the surface area S are ordered in the same way keeping in mind that D is very similar for Al and Ni-Cr. Said differently our study reveals a strong link between the fractal dimension of the vacuum arc cathode spots and the covered area: a large D corresponds to a large S . This was expected in fact as the fractal dimension characterizes the space-filling capacity of a pattern.

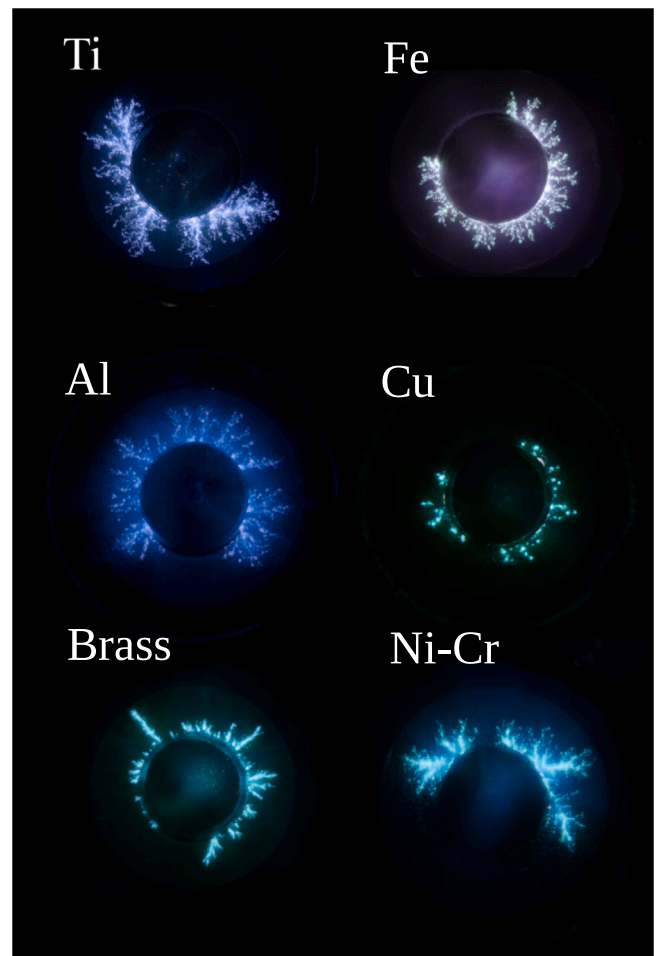


Fig. 8. Raw photograph of cathodic arcs using different materials.

Table 5
Mean surface area covered by spots for different cathode materials.

Material	S (mm ²)	σ_S	% of the cathode area
Ti	4.2	0.4	11.1
Ni-Cr	3.2	0.3	8.5
Al	2.6	0.4	6.9
Fe	2.4	0.3	6.3
Brass	1.4	0.1	3.7
Cu	0.9	0.09	2.3

Results are similar when comparing a fresh and a worn cathode: the covered area does not depend on the wear degree. Table 4 shows that the value of S is about 4.4 mm^2 in the case of a titanium cathode whatever the cathode surface state. Fig. 8 shows in addition an interesting characteristic of the arc discharge. There is always a sector of the cathode with no arcs and spots. The sector location and size change from one pulse to the other. Empty sectors have been observed for all photographs for the six tested materials. The existence of such sectors and their dynamics remain unexplained. They, however, participate in the fact that the area covered by the arcs is a small fraction of the total cathode area as illustrated in Table 5.

3.5. Discussion

The dendritic aspect of the traces left on cathode surfaces has been consistently observed either on metal plates [2] or on films [5]. Note that for studies described in Refs. [2,3] vacuum arcs were operating at 50 A, a current magnitude much below the one of the PJP thruster. Striking similarities were found between the cathode spots patterns and Lichtenberg figures, or even structures obtained by diffusion-limited aggregation [23]. In our work, despite the fact that the discharge current I_d is almost 100 times higher, fractal patterns are still identified, especially when taking a close view to the dendrites. Similarities come from the fact that a spot cell can sustain a limited current density j [24]. When j becomes too high, another spot is initiated elsewhere and j decreases as the current flows through two different spot cells. Hence, the number of spots increases linearly with I_d [25]. On the other hand, cathode spots have a limited lifetime which is proportional to j^2 . At the end of its lifetime, the spot extinguishes and another one ignites elsewhere. This sequence of ignitions and extinctions spreads over the cathode surface in a random walk process [3,26]. Note that the random walk in the case of vacuum arcs is not necessary a self avoiding walk, which means that a previously active spot may reignite later. Photographs taken in this study certainly contain spots that have been ignited several times. As spot and vacuum arc dynamics is governed by the current density, it is not surprising that high-current short duration arcs show structural similarities with low-current long duration arcs when the photograph exposure time is longer than the discharge duration in such a way all spots have been captured. The main difference between low- and high-current arcs is just the number of simultaneously active spots [21].

The size of a group of spots, generally speaking, is closely related to the pre-explosion specific action of the cathode material [10,27]. This parameter h is written in wire explosion theory as :

$$h = \int_{t_0}^{t_{br}} j^2 dt \quad (2)$$

where t_0 is the time at which the energy is released in the circuit, t_{br} the instant the explosion occurs and j is the current density. This quantity represents the “thermal toughness” of the material heated with a current pulse [28,29]. This parameter h has been linked to the ecton formation criterion in several studies [24,30]. The ecton can be seen in this case as a potential candidate to the physical spatial cutoff of the fractal structure. It should be emphasized that in the present contribution, the spatial cutoff is the pixel size. It has been shown in [10] that h strongly depends on the cathode material, in such a way that it can be considered a function of the cathode material only, regardless of the energy input in the discharge or the cathode temperature. Unfortunately, values of h are not available in the literature neither for pure metals nor for alloys. Therefore h could not be accounted for the fractal dimension analysis. However, it confirms that the structure of the plasma emission sites strongly depends on the cathode material for a similar geometry. It is therefore of interest to examine the physical properties of the different cathode materials. The objective is here twofold, namely: (i) to find which material properties influence the most the cathode spot structure during a plasma discharge and (ii) to reveal a possible relation between the fractal dimension of the vacuum arc cathode spots and cathode material characteristics.

4. Influence of material properties

To the best of the authors knowledge, there is currently no equation ruling the evolution of the fractal dimension with the cathode material properties. This work shows, however, that when applying the same voltage and releasing the same energy in the discharge for the same cathode geometry, the fractal dimension and the covered area are material-dependent. This idea is supported by the fact that the ordering in D and S follows the ordering of the mean diameter of macropoints in [21], for titanium, aluminum and copper, despite different experimental conditions. Two different yet complementary approaches, namely Machine Learning and Heuristic method are proposed here to investigate the impact of the cathode material on the arc pattern.

The physical properties considered in these two approaches are the following: thermal conductivity λ [W/(m K)], electrical conductivity σ [S/m], density ρ [kg/m³], vaporization energy E_{vap} [kJ/mol], cohesive energy, E_{coh} [kJ/mol], ionization energy E_{ion} [kJ/mol] and work function W_f [kJ/mol]. Values have been taken from the handbook of chemistry and physics [31] as well as from [32] and are presented in Table 6. Exact values of energies for alloys could not be found from the literature. Therefore the weighted average with respect to the composition of the alloy was used. According to several works [33–37] such an approximation is reasonable.

4.1. Machine learning

In order to determine a relation between the material properties and the fractal dimension D , an approach based on machine learning (ML) has first been considered as it allows to quantify each term contribution to the prediction function. Such insight is useful to capture the most contributing physical properties to the change in fractal dimension. The numerical model consists in a multivariate polynomial regression (MPR). A correlation between the fractal dimension and relevant material properties is sought in the form

$$D = \sum_k \sum_i \alpha_{i,k} x_i^k \quad \text{with } \alpha_{i,k} \geq 0 \quad (3)$$

where D is the predicted fractal dimension, $\alpha_{i,k}$ are linear coefficients and x_i are physical constants relative to the cathode material, here extracted from Table 6. Each x_i appears in the expression with exponent k . As for the polynomial order, since most scaling laws in physics feature exponents ± 0.5 , ± 1 and/or ± 2 , it is chosen to limit k to these values. No intercept is allowed in the model shown in Eq. (3), which means that a null fractal dimension is assumed when all physical properties are equal to zero. Physically, it means that no discharge can occur without a propagation medium.

The analysis consists in determining the value of each $\alpha_{i,k}$ that outputs the best fit to the experimentally observed fractal dimension. For this purpose, a ML program was developed in Python. Having selected 7 physical properties and 6 exponents, 42 coefficients are to be determined. In practical terms, the algorithm targets at minimizing the residual sum of squares between the experimentally observed fractal dimension and the one retrieved by the polynomial approximation. The dataset on which the analysis is performed comprises 6 materials and 411 pictures. This is randomly split into a training set (85%) and a test set (15%). The training and test sets are depicted in Fig. 9 along with the fractal dimension predicted by the ML program. The quality of the model is quantitatively assessed on the test set through the MAE and R^2 metrics, which read 2.15% and 0.94, respectively. These parameters outline that the model does satisfactorily predict the experimental findings.

Fig. 10 shows the normalized values of every $\alpha_{i,k} x_i^k$ for the six tested materials, that means their respective contribution to the fractal dimension prediction function. In all cases, the reciprocal of the work function term contribute more than 55% to the fractal dimension. The sum of the squared ionization energy and squared cohesive energy

Table 6
Physical properties of cathode materials considered in this study.

Material	λ [W/(m K)]	$\sigma \times 10^6$ [S/m]	$\rho \times 10^3$ [kg/m ³]	E_{coh} [kJ/mol]	E_{vap} [kJ/mol]	E_{ion} [kJ/mol]	W_f [kJ/mol]
Ti	22	2.34	4.51	468	421	659	418
Al	237	37.7	2.69	327	293	577	402
Ni-Cr	11	0.93	8.55	421 ^a	365 ^a	721 ^a	488 ^a
Fe	80	9.93	7.87	413	350	762	457
Brass	125	15.6	8.45	259 ^a	231 ^a	803 ^a	419 ^a
Cu	401	59.6	8.96	336	300	746	459

^aAverage between the properties of the materials composing the alloy

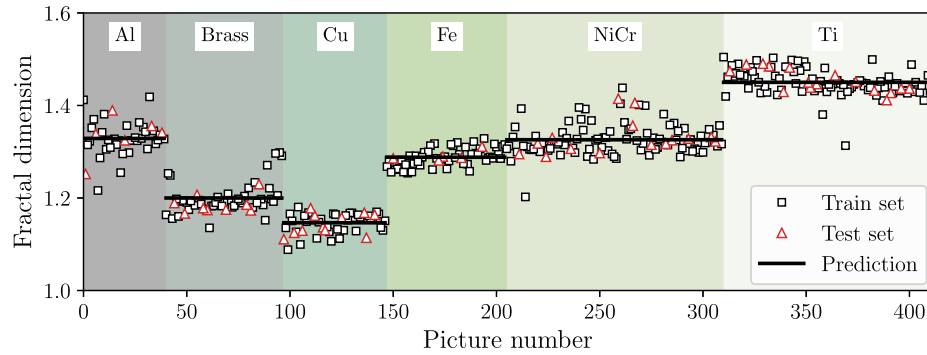


Fig. 9. Scatter plot of train set, test set and predicted value of fractal dimension.

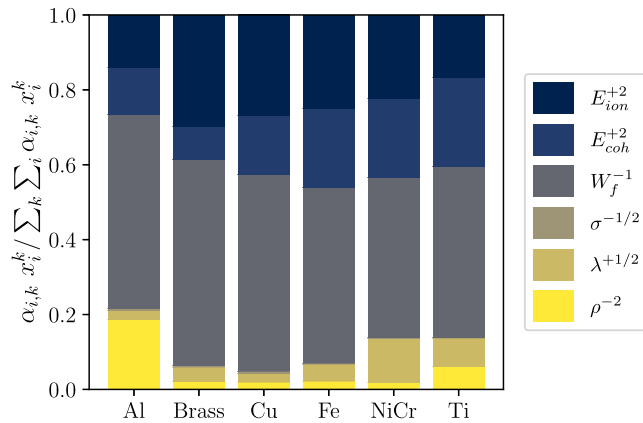


Fig. 10. Normalized cumulative bar plot of the absolute value of each $\alpha_{i,k} x_i^k$. Omitted units are consistent with Table 6.

accounts for more than 35%, with varying proportions. The remaining quantities visible at the bottom of Fig. 10 appear with variable weights depending on how the dataset is randomly divided into train and test sets. This effect possibly results from the relatively limited amount of data available. Therefore the precise influence of ρ , λ and σ is difficult to quantify with this approach, however it certainly remains secondary. Note that the contribution of the vaporization energy is null in each case.

4.2. Heuristic approach

As a means to complete the ML model and examine whether a product relation between the material properties can also explain the change of fractal dimension D , a heuristic analysis has been implemented. It relies here on an expression in the form

$$D \propto \prod_i x_i^k \quad (4)$$

where x_i is a physical parameter relative to the cathode material and k are usual exponents in physical laws, in a similar fashion to the

approach discussed beforehand. Values of k are limited once again to $k = 0, \pm 0.5, \pm 1, \pm 2$. As this approach relies on an expression in a product form, a risk of overfitting the data can arise. One should then limit the number of x_i 's. In that respect, since the ML model brings out the main contributing properties, the method proposed here only considers parameters with a contribution above 10% in the ML model i.e. E_{coh} , E_{ion} and W_f . Note however that the heuristic model considers a product of the various physical properties while the ML model is based on a sum. All the 343 possible combinations have been tested in an iterative way for the six materials using a custom program in Python. For each combination a linear regression analysis is performed that includes the six materials. Unlike with the previous model, the intercept of the linear regression is not forced to be null. The expression giving both the lowest mean absolute error (MAE) and the highest R^2 is considered the most probable and the most appropriate relation of proportionality between the physical parameters of the material and the fractal dimension. Following this procedure, the best suited relation between D and the material properties is:

$$D \propto \frac{E_{coh}^2}{W_f E_{ion}^2} \quad (5)$$

The evolution of the fractal dimension D with this combination of parameters is displayed in Fig. 11. With the relation given by Eq. (5), the linear regression yields a mean absolute error of 0.025 and a R^2 equal to 0.865. It is quite clear from this figure that the copper is responsible for the decrease in R^2 . The linear regression without taking Cu into account has an R^2 of 0.987. This may be due to the accuracy of the box counting method with the copper dataset. The copper spots covering the smallest surface with small filaments, the box counting algorithm is less accurate as the size of the spot pattern is close to the pixel size.

The five relations having the most linear behavior, as well as the coefficients of the regression and their respective R^2 and MAE, are given and ranked in Table 7. This table indicates that the cohesive energy increases the fractal dimension while the work function and the ionization energy decreases D . Studies have shown that the noise amplitude in the vacuum arc burning voltage scales linearly with the cohesive energy of the cathode material [38,39]. According to the theory of colored noise [40,41], this noise in burning voltage could

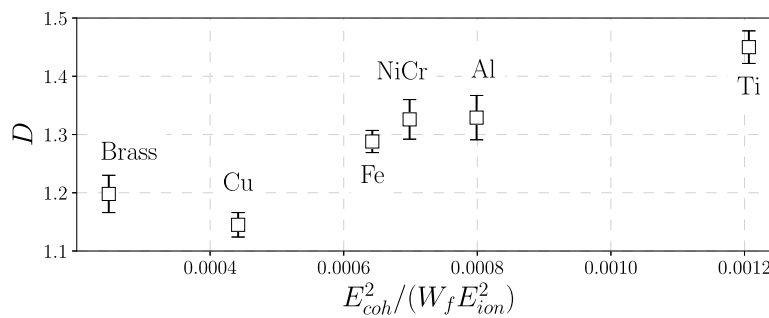


Fig. 11. Evolution of the fractal dimension according to Eq. (5).

Table 7

Most appropriate relations of proportionality between the physical parameters of the material and the fractal dimension.

Relation	a	b	R^2	MAE
$\frac{E_{coh}^2}{W_f E_{ion}^2}$	305.7	1.08	0.865	0.025
$\frac{E_{coh}}{W_f \sqrt{E_{ion}}}$	13.4	0.86	0.841	0.030
$\frac{E_{coh}}{W_f^2 \sqrt{E_{ion}}}$	5096.8	0.91	0.813	0.030
$\frac{E_{coh}}{W_f^2 E_{ion}}$	111107.8	0.98	0.771	0.039
$\frac{\sqrt{E_{coh}}}{W_f^2}$	5616.3	0.72	0.623	0.049

possibly indicate a Brownian motion of the active cathode spots, often approximated with random walk models. A link could therefore be expected between the spot distribution over the cathode surface and the cohesive energy of the cathode material. On the other hand, the ionization energy and the work function counteract the cohesive energy in the relation, playing a crucial role in reducing the fractal dimension magnitude.

5. Conclusion

Photographs of cathode spots taken during firing of a high current vacuum arc thruster reveal a fractal structure on the cathode surface. The dimension of these structures was determined by the Minkowski–Bouligand method. It was found that the fractal dimension varies considerably as a function of the cathode material. Differences cannot be attributed to the typical dispersion resulting from several separated discharges, or to surface conditions. For the same energy released in the discharge, D spreads from 1.14 ± 0.02 for copper to 1.45 ± 0.03 for titanium. The total surface covered by the spots during a discharge shows the same variation and the same ordering.

Two methods have been proposed to investigate the role of the cathode material physical properties in relation to both the fractal dimension and the total surface. A machine learning approach as well as a heuristic analysis show that the work function, the ionization energy and the cohesive energy of the material play an important role in the fractal pattern. Variation of D as a function of the cathode material could be further examined by extending the investigation to materials with large and small E_{coh} respectively.

Numerous studies have been carried out in the past about cathode spots of vacuum arcs fractal. This work however proposes a quite unique arc regime in terms of current intensity and pulse duration as well as an unusual application in the field of satellite propulsion. In addition to determine the arc fractal dimension for several cathode materials, we also investigate the relation between D and the material

physical properties and we suggest an ordering. This work is not an end in itself, just a step towards a broader and more meaningful conclusion as the ultimate goal is to identify a possible relation between the fractal dimension and the VAT performances in terms of specific impulse, impulse bit and thrust efficiency. A link between fractal dimension, cathode material properties and performances would certainly help researchers and engineers in the development and optimization of thrusters and offer paths for better understanding the complex physics at play. Looking for a relationship between D and thruster performances requires thrust measurements, that means the building of a dedicated thrust balance. We are currently working on that specific point. Measurements performed by the PJP thruster manufacturer nevertheless indicate the thrust is large with a titanium cathode and much smaller when copper is used, what we would expect if thrust is driven by the fractal dimension.

CRedit authorship contribution statement

Etienne Michaux: Writing – review & editing, Writing – original draft, Software, Methodology, Investigation, Conceptualization. **Alfio E. Vinci:** Writing – review & editing, Writing – original draft, Software, Methodology, Conceptualization. **Stéphane Mazouffre:** Writing – review & editing, Writing – original draft, Validation, Supervision, Conceptualization.

Declaration of competing interest

The authors declare that they have no known competing financial interests or personal relationships that could have appeared to influence the work reported in this paper.

Data availability

Data will be made available on request.

Acknowledgments

This project was supported by the European Union’s Horizon 2020 research and innovation program under grant agreement n° 870444 (Plasma Jet Pack). Authors would like to thank C. Chauveau for the lending of high-quality optics.

References

- [1] L. Niemeyer, L. Pietronero, H. Wiesmann, Fractal dimension of dielectric breakdown, Phys. Rev. Lett. 52 (12) (1984) 1033, <http://dx.doi.org/10.1103/PhysRevLett.52.1033>.
- [2] A. Anders, The fractal nature of vacuum arc cathode spots, IEEE Trans. Plasma Sci. 33 (5) (2005) 1456–1464, <http://dx.doi.org/10.1109/TPS.2005.856488>.
- [3] J. Daalder, Random walk of cathode arc spots in vacuum, J. Phys. D: Appl. Phys. 16 (1) (1983) 17, <http://dx.doi.org/10.1088/0022-3727/16/1/005>.
- [4] B. Juttner, H. Pursch, V. Shilov, The influence of surface roughness and surface temperature on arc spot movement in vacuum, J. Phys. D: Appl. Phys. 17 (2) (1984) L31, <http://dx.doi.org/10.1088/0022-3727/17/2/002>.

- [5] S. Anders, B. Juttner, Influence of residual gases on cathode spot behavior, *IEEE Trans. Plasma Sci.* 19 (5) (1991) 705–712, <http://dx.doi.org/10.1109/27.108402>.
- [6] S. Barengolts, G. Mesyats, D. Shmelev, Structure and time behavior of vacuum arc cathode spots, *IEEE Trans. Plasma Sci.* 31 (5) (2003) 809–816, <http://dx.doi.org/10.1109/TPS.2003.818449>.
- [7] A. Blanchet, L. Herrero, L. Voisin, B. Pilloy, D. Courteville, Plasma jet pack technology for nano-microsatellites, in: *36th International Electric Propulsion Conference*, 2019.
- [8] E. Michaux, S. Mazouffre, A. Blanchet, Time evolution of plasma parameters in the jet of a low-power vacuum arc thruster, *J. Electr. Propul.* 1 (1) (2022) 1–16, <http://dx.doi.org/10.1007/s44205-022-00007-w>.
- [9] E. Michaux, S. Mazouffre, R. Fritzsche, Spatial and temporal 2 evolution of ion and electron parameters in the plasma jet of a 30W VAT, in: *Proceedings of the 37th International Electric Propulsion Conference*, 2022.
- [10] G. Mesyats, Ecton or electron avalanche from metal, *Phys.-Usp.* 38 (6) (1995) 567, <http://dx.doi.org/10.1070/PU1995v038n06ABEH000089>.
- [11] D. Alpert, D. Lee, E. Lyman, H. Tomaschke, Initiation of electrical breakdown in ultrahigh vacuum, *J. Vac. Sci. Technol.* 1 (2) (1964) 35–50, <http://dx.doi.org/10.1116/1.1491722>.
- [12] M. Keidar, J. Schein, K. Wilson, A. Gerhan, M. Au, B. Tang, L. Idzkowski, M. Krishnan, I. Beilis, Magnetically enhanced vacuum arc thruster, *Plasma Sources. Sci. Technol.* 14 (4) (2005) 661, <http://dx.doi.org/10.1088/0963-0252/14/4/004>.
- [13] I. Beilis, *Plasma and Spot Phenomena in Electrical Arcs*, vol. 113, Springer Nature, 2020, <http://dx.doi.org/10.1007/978-3-030-44747-2>.
- [14] I. Beilis, Vacuum arc cathode spot theory: history and evolution of the mechanisms, *IEEE Trans. Plasma Sci.* 47 (8) (2019) 3412–3433, <http://dx.doi.org/10.1109/TPS.2019.2904324>.
- [15] K. Falconer, *Fractal Geometry: Mathematical Foundations and Applications*, John Wiley & Sons, 2004.
- [16] A. Husain, J. Reddy, D. Bisht, M. Sajid, Fractal dimension of coastline of Australia, *Sci. Rep.* 11 (1) (2021) 1–10, <http://dx.doi.org/10.1038/s41598-021-85405-0>.
- [17] N. Rougier, J.B. Hamrick, G. ibah, D. Heverly-Coulson, C. Deil, B. Telenczuk, *Numpy-100: Version 1.1*, 2016, <http://dx.doi.org/10.5281/zenodo.61020>.
- [18] K. Oh, D. Kalanov, A. Anders, High-resolution observation of cathode spots in a magnetically steered vacuum arc plasma source, *Plasma Sources. Sci. Technol.* 30 (9) (2021) 095005, <http://dx.doi.org/10.1088/1361-6595/ac1ee1>.
- [19] K. Oh, D. Kalanov, P. Birtel, A. Anders, High-resolution observation of cathodic arc spots in a magnetically steered arc plasma source in low pressure argon, nitrogen, and oxygen atmospheres, *J. Appl. Phys.* 130 (18) (2021) 183304, <http://dx.doi.org/10.1063/5.0072021>.
- [20] M. Golizadeh, A. Anders, F. Mendez Martin, S. Kolozsvári, R. Franz, Insights into surface modification and erosion of multi-element arc cathodes using a novel multilayer cathode design, *J. Appl. Phys.* 127 (11) (2020) 113301, <http://dx.doi.org/10.1063/1.5141406>.
- [21] P. Siemroth, T. Schulke, T. Witke, Investigation of cathode spots and plasma formation of vacuum arcs by high speed microscopy and spectroscopy, *IEEE Trans. Plasma Sci.* 25 (4) (1997) 571–579, <http://dx.doi.org/10.1109/27.640667>.
- [22] T. Schulke, P. Siemroth, Vacuum arc cathode spots as a self-similarity phenomenon, *IEEE Trans. Plasma Sci.* 24 (1) (1996) 63–64, <http://dx.doi.org/10.1109/27.491692>.
- [23] T. Witten Jr., L. Sander, Diffusion-limited aggregation, a kinetic critical phenomenon, *Phys. Rev. Lett.* 47 (19) (1981) 1400, <http://dx.doi.org/10.1103/PhysRevLett.47.1400>.
- [24] G. Mesyats, S. Barengolts, The cathode spot of a high-current vacuum arc as a multiecton phenomenon, *IEEE Trans. Plasma Sci.* 29 (5) (2001) 704–707, <http://dx.doi.org/10.1109/27.964458>.
- [25] B. Djakov, R. Holmes, Cathode spot division in vacuum arcs with solid metal cathodes, *J. Phys. D: Appl. Phys.* 4 (4) (1971) 504, <http://dx.doi.org/10.1088/0022-3727/4/4/305>.
- [26] A. Anders, The evolution of ion charge states in cathodic vacuum arc plasmas: a review, *Plasma Sources. Sci. Technol.* 21 (3) (2012) 035014, <http://dx.doi.org/10.1088/0963-0252/21/3/035014>.
- [27] S. Barengolts, G. Mesyats, D. Shmelev, Mechanism of ion flow generation in vacuum arcs, *J. Exp. Theor. Phys.* 93 (5) (2001) 1065–1073.
- [28] Y. Kotov, Electric explosion of wires as a method for preparation of nanopowders, *J. Nanopart. Res.* 5 (5) (2003) 539–550, <http://dx.doi.org/10.1023/B:NANO.0000006069.45073.0b>.
- [29] L. Chemezova, G. Mesyats, V. Sedoi, B. Semin, V. Valevich, The integral of specific current action and the specific energy input under fast electrical explosion, in: *Proceedings ISDEIV. 18th International Symposium on Discharges and Electrical Insulation in Vacuum* (Cat. No. 98CH36073), vol. 1, IEEE, 1998, pp. 48–51, <http://dx.doi.org/10.1109/DEIV.1998.740570>.
- [30] G. Mesyats, *Pulsed Power*, Springer Science & Business Media, 2007, <http://dx.doi.org/10.1007/b116932>.
- [31] W. Haynes, D. Lide, T. Bruno, *CRC Handbook of Chemistry and Physics*, CRC Press, 2016, <http://dx.doi.org/10.1201/9781315380476>.
- [32] E. Kaxiras, *Atomic and Electronic Structure of Solids*, Cambridge University Press, 2003, <http://dx.doi.org/10.1017/CBO9780511755545>.
- [33] M. Akbi, A. Bouchou, M. Ferhat-Taleb, Effects of surface treatments on photoelectric work function of silver–nickel alloys, *Vacuum* 101 (2014) 257–266, <http://dx.doi.org/10.1016/j.vacuum.2013.09.003>.
- [34] A. Gangopadhyay, J. Bendert, N. Mauro, K. Kelton, Inverse correlation between cohesive energy and thermal expansion coefficient in liquid transition metal alloys, *J. Phys.: Condens. Matter* 24 (37) (2012) 375102, <http://dx.doi.org/10.1088/0953-8984/24/37/375102>.
- [35] M. Turchanin, P. Agraval, Cohesive energy, properties, and formation energy of transition metal alloys, *Powder Metall. Metal Ceram.* 47 (1) (2008) 26–39, <http://dx.doi.org/10.1007/s11106-008-0006-3>.
- [36] L. Zhan, Z. Xu, Separating and recycling metals from mixed metallic particles of crushed electronic wastes by vacuum metallurgy, *Environ. Sci. Technol.* 43 (18) (2009) 7074–7078, <http://dx.doi.org/10.1021/es901667m>.
- [37] A. Watson, F. Hayes, Enthalpies of formation of solid Ni–Cr Ni–Cr and Ni–V alloys by direct reaction calorimetry, *J. Alloys Compd.* 220 (1–2) (1995) 94–100, [http://dx.doi.org/10.1016/0925-8388\(94\)06008-8](http://dx.doi.org/10.1016/0925-8388(94)06008-8).
- [38] A. Anders, E. Oks, G. Yushkov, Cathodic arcs: Fractal voltage and cohesive energy rule, *Appl. Phys. Lett.* 86 (21) (2005) 211503, <http://dx.doi.org/10.1063/1.1937994>.
- [39] E. Oks, I. Brown, Emerging applications of vacuum-arc-produced plasma, ion and electron beams, 2003, <http://dx.doi.org/10.1007/978-94-010-0277-6>.
- [40] M. Schroeder, *Fractals, Chaos, Power Laws: Minutes from an Infinite Paradise*, Courier Corporation, 2009, <http://dx.doi.org/10.1063/1.2810323>.
- [41] A. Osborne, A. Pastorello, Simultaneous occurrence of low-dimensional chaos and colored random noise in nonlinear physical systems, *Phys. Lett. A* 181 (2) (1993) 159–171, [http://dx.doi.org/10.1016/0375-9601\(93\)90914-L](http://dx.doi.org/10.1016/0375-9601(93)90914-L).